

MesoMem: A mesoscale membrane model based on an additive potential

Pietro Sillano

*Department of Bionanoscience, Kavli Institute of Nanoscience,
Delft University of Technology, Delft, The Netherlands and
Molecular Dynamics Group, Groningen Biomolecular Sciences and
Biotechnology Institute, University of Groningen, The Netherlands*

Siewert Jan Marrink

*Molecular Dynamics Group, Groningen Biomolecular Sciences and
Biotechnology Institute, University of Groningen, The Netherlands*

Timon Idema*

*Department of Bionanoscience, Kavli Institute of Nanoscience,
Delft University of Technology, Delft, The Netherlands*

(Dated: March 2, 2026)

Bridging the gap between atomistic detail and continuum mechanics is a central challenge in modeling biological membranes, particularly for mesoscopic phenomena spanning large length and time scales. In this work, we introduce a new, solvent-free, one-particle-thick, coarse-grained model for lipid bilayers, governed by an additive potential. Our approach treats orientational elasticity through distinct additive energy terms for tilt and splay, offering an unbiased potential form. The model is implemented in the LAMMPS molecular dynamics engine. Our simulations show spontaneous self-assembly of lamellar structures and stable vesicles from disordered states. We map the dynamical phase diagram of the system, identifying distinct gel-like, fluid, and gas regimes, controlled by temperature and the steepness of the isotropic attraction. The model accurately reproduces the theoretical $1/q^4$ fluctuation spectrum for tensionless membranes and exhibits tunable mechanical properties, including biologically relevant bending rigidities and area compressibility moduli. We show how we can include osmotic pressure and spontaneous curvature in our model. Finally, we demonstrate the model's applicability to complex membrane remodeling by simulating the adhesive wrapping of colloidal nanoparticles, recovering the predicted dependency on particle size and adhesion strength.

I. INTRODUCTION

Biological membranes are essential structural elements of living systems. They provide the boundaries of cells and organelles, mediate selective transport, and act as active participants in mechanical and biochemical processes [1]. From a physical perspective, membranes are thin, flexible surfaces with rich collective behavior, encompassing thermal undulations, curvature generation, and large-scale morphological transformations such as budding and fusion [2]. Capturing this complexity in a computational framework remains a central challenge in soft matter physics. The primary difficulty arises from the wide separation of length and time scales that characterize membrane dynamics. Events at the membrane range from the nanosecond dynamics of individual lipid molecules to the microsecond-to-second timescales of protein diffusion and macroscopic domain formation, and ultimately to the cellular-level processes that happen over minutes or even longer.

Atomistic molecular dynamics provides an accurate description of interactions, but is computationally limited to relatively small systems and short timescales. At the

other end of the spectrum, continuum elasticity models effectively describe large-scale shapes and bending energetics, but lack explicit microscopic degrees of freedom. Bridging these extremes requires coarse-grained strategies that reduce molecular detail while retaining local interactions, enabling simulations of mesoscopic membrane behavior. Coarse-grained force fields such as Martini [3], the Cooke-Deserno model [4] or the model developed in the Voth group [5] simplify the lipid molecule description. While these allow for significantly larger spatial and temporal scales than atomistic modeling, they still explicitly simulate individual lipids. For example, the Martini model can effectively capture microsecond dynamics for assemblies of approximately $10^5 - 10^6$ lipids, *i.e.*, roughly a square micrometer [3]. To access larger spatio-temporal length scales, necessary to accurately simulate the dynamics of entire organelle or Giant Unilamellar Vesicles (GUV) systems, we must shift to highly coarse-grained, or 'mesoscopic', descriptions.

These mesoscopic models generally fall into two categories: mesh-based and particle-based. In both approaches, the fundamental discretization unit (a vertex or a bead) corresponds to a lipid patch several nanometers in size. Mesh-based models represent the membrane as a discretized, triangulated surface. These discretized models often employ a Monte Carlo scheme to sample the equilibrium configuration of the system [6–8]. Con-

* t.idema@tudelft.nl

versely, solvent-free particle-based models at the mesoscopic level are based on molecular or Brownian dynamics [9–11]. These models have been used to simulate large-scale planar membranes or vesicles [12, 13], interacting with colloidal particles [14] and coarse-grained filaments [15] or proteins [16]. Despite sharing a common mesoscopic scale, the constitutive units of the two most used models differ fundamentally. The model of Yuan *et al.* [9] utilizes a one-particle-thick representation, where a single anisotropic bead corresponds to a bilayer patch; its dynamics are governed by pairwise interactions scaled by a multiplicative orientation term. In contrast, Noguchi [10] models the bilayer as two coupled monolayers, employing a more complex additive potential that sums separate energetic terms for particle density and orientational alignment.

In this work, we introduce a new coarse-grained particle model operating in the mesoscopic regime, combining the simplicity of a single-particle-thick representation with an additive treatment of orientation-dependent interactions, thereby offering an alternative to the multiplicative scheme of Yuan *et al.* and the bilayer-based construction of Noguchi. Our motivation arises from the need for a computationally efficient single-bead description of the membrane bilayer, the intention to provide an openly available and easily adoptable implementation, and the objective of establishing an unbiased potential form for particle interactions.

In this paper we present the formulation and derivation of the model and provide an implementation for the popular Molecular Dynamics (MD) engine LAMMPS [17]. We will demonstrate our model’s capability to capture essential membrane behaviors, including self-assembly and the correct prediction of the fluctuation spectrum for planar membranes.

II. METHODS

A. Model potential

The membrane is represented as a one-particle-thick sheet of coarse-grained elements. Each particle corresponds to a patch of lipid bilayer with an area of a few nanometer squared and is modeled as a point-like dipole with an orientation vector \hat{n}_i representing the local membrane normal. The model is additive in form and the solvent is modeled implicitly. All quantities are expressed in Lennard Jones (LJ) reduced units, with particle mass $m = 1$, particle diameter σ and energy scale ε (the depth of the LJ well). Tilt k_{tilt} and splay k_{splay} moduli are expressed in units of energy ε . The time unit will be $\tau_{\text{LJ}} = \sqrt{\varepsilon/m\sigma^2}$.

The total energy is written as

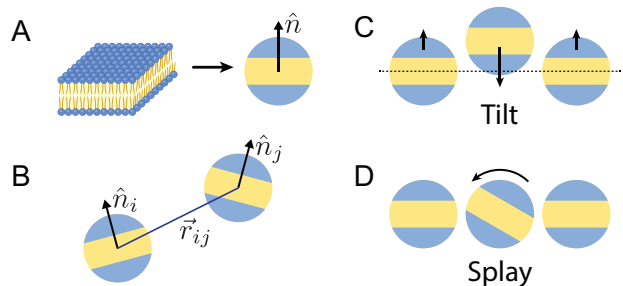


FIG. 1: Schematic of the model and interaction geometry. (A) Representation of a lipid bilayer patch as a single coarse-grained particle. The particle has rotational symmetry. (B) The separation vector \vec{r}_{ij} , and normal vectors \hat{n}_i and \hat{n}_j used in the derivation of the potential. (C) Schematic illustrating the forces resulting from a tilt deformation. (D) Schematic illustrating the torques resulting from a splay deformation.

$$\begin{aligned}
 H &= U_{\text{rep}} + U_{\text{attr}} + U_{\text{tilt}} + U_{\text{splay}} \\
 &= \sum_{i < j} \left\{ U_{\text{rep}}(r_{ij}) + U_{\text{attr}}(r_{ij}) \right. \\
 &\quad \left. + \left[U_{\text{tilt}}(\hat{n}_i, \hat{n}_j, \hat{r}_{ij}) + U_{\text{splay}}(\hat{n}_i, \hat{n}_j) \right] w(r_{ij}) \right\}, \quad (1)
 \end{aligned}$$

where $\vec{r}_{ij} = \vec{r}_i - \vec{r}_j$, $r_{ij} = |\vec{r}_{ij}|$, and $\hat{r}_{ij} = \vec{r}_{ij}/r_{ij}$.

a. Isotropic interactions. Particles interact through a soft core excluded-volume repulsion combined with a short range attraction, see Fig. 2. The repulsive branch is given by a 4–2 LJ potential,

$$U_{\text{rep}}(r) = \varepsilon \left[\left(\frac{r_{\text{min}}}{r} \right)^4 - 2 \left(\frac{r_{\text{min}}}{r} \right)^2 \right], \quad r \leq r_{\text{min}}, \quad (2)$$

with cutoff at the potential minimum $r_{\text{min}} = 1.0 \sigma$. The softer 4–2 form, compared to the conventional 12–6 LJ potential, avoids crystallization behavior.

The attractive branch is described by a smoothly truncated cosine-squared potential,

$$U_{\text{attr}}(r) = \begin{cases} -\varepsilon \cos^2 \zeta \left(\frac{\pi(r - r_{\text{min}})}{2(r_c - r_{\text{min}})} \right), & r_{\text{min}} < r < r_c, \\ 0, & r \geq r_c, \end{cases} \quad (3)$$

which guarantees a continuous decay to zero at r_c and avoids force discontinuities. The exponent ζ tunes the slope and the width of the attractive branch of the potential. The cut-off distance is also a model parameter tuning system behavior; in standard conditions we set its value to $r_c = 2.5\sigma$, such that each particle is interacting with two shells of neighbors. Together these terms provide tunable short-range attraction with soft excluded volume, consistent with the previous one-particle-thick membrane model of Yuan *et al.* [9].

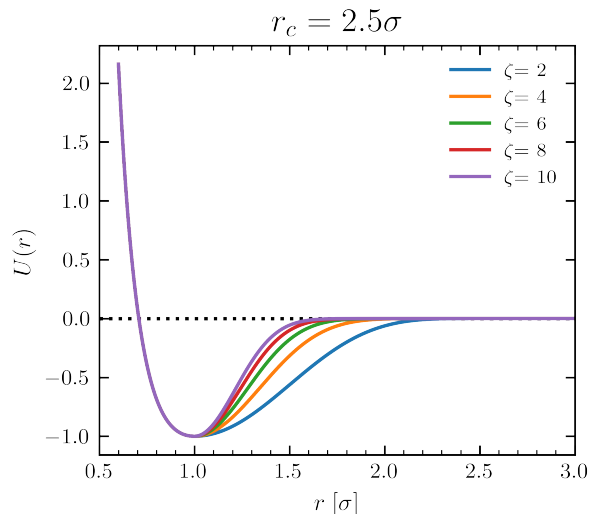


FIG. 2: Isotropic potential $U(r)$ with isotropic cutoff $r_c = 3.0$. The ζ parameter is tuning the slope of the attractive branch of the potential.

b. Anisotropic interactions. We introduce local orientational elasticity through tilt and splay interactions, which serve as a discretized version of the tilt model [18]. The tilt term penalizes the deviation of particle directors from the local surface normal, whereas the splay term suppresses misalignment between neighboring particles.

The tilt energy for a particle pair is defined as:

$$U_{\text{tilt}} = \frac{k_{\text{tilt}}}{2} [(\hat{n}_i \cdot \hat{r}_{ij})^2 + (\hat{n}_j \cdot \hat{r}_{ij})^2]. \quad (4)$$

This potential is minimized when particle orientations are orthogonal to the interparticle axis \vec{r}_{ij} , consistent with a flat bilayer configuration. Physically, this interaction generates both translational forces and rotational torques.

To ensure orientational coherence across the bilayer, the splay energy is given by:

$$U_{\text{splay}} = \frac{k_{\text{splay}}}{2} (\hat{n}_i \cdot \hat{n}_j - 1)^2. \quad (5)$$

This term favors parallel (or antiparallel) alignment of neighboring dipoles. Unlike the tilt term, the splay interaction generates only torques.

c. Weighting function. Tilt and splay interactions act only within a finite range and are modulated by a smooth cutoff function [10]:

$$w(r) = \begin{cases} \exp\left(\frac{(r/r_{\text{ga}})^2}{(r/w_c)^n - 1}\right), & r \leq w_c, \\ 0, & r \geq w_c, \end{cases} \quad (6)$$

typically with $n = 4$ and $r_{\text{ga}} = 1.5\sigma$. The freely adjustable parameter w_c is used to set the effective range of orientational interactions.

d. Implementation. Forces and torques are evaluated pairwise, with explicit derivations provided in the supplementary material. The model has been implemented in LAMMPS [17] writing a novel custom pair-style. The source code is openly available in our Gitlab repository: <https://gitlab.tudelft.nl/idemagroup/mesomem>.

B. Langevin dynamics

We simulated the membrane in the NVT ensemble (constant number of molecules N , volume V , and temperature T) with periodic boundary conditions in a box with sides of length L_x , L_y and L_z .

To model the effect of an implicit solvent, we employed Langevin dynamics, in which translational and rotational motion are damped by frictional forces and subject to stochastic thermal noise. The damping serves two purposes: (i) it mimics the viscous drag exerted by the solvent on the particles, and (ii) it stabilizes particle orientations, ensuring correct alignment and structural integrity of the membrane.

The translational dynamics of each particle is described by

$$m\ddot{\vec{r}}_i = -\vec{F}_i - \gamma_t \dot{\vec{r}}_i + \vec{\eta}_i^t, \quad (7)$$

where m is the particle mass, \vec{F}_i are conservative forces, γ_t the translational friction coefficient, and $\vec{\eta}_i^t$ a Gaussian random force with zero mean and variance determined by the fluctuation-dissipation relation.

The rotational dynamics uses a rotation vector representation (as implemented in LAMMPS) to integrate the unit orientation \hat{n}_i :

$$I\ddot{\hat{n}}_i = -\vec{T}_i - \gamma_r \dot{\hat{n}}_i + \vec{\eta}_i^r, \quad (8)$$

with $I = \frac{2}{5}m\sigma^2$ the moment of inertia of a spherical particle of radius σ , \vec{T}_i are conservative torques, γ_r the rotational friction coefficient, and $\vec{\eta}_i^r$ a Gaussian random torque. The rotation vector formalism ensures that the orientation remains normalized during integration.

We model the thermal bath using Gaussian white noise. Both the random forces and torques have a zero mean, meaning they do not drive the system in any specific direction:

$$\begin{aligned} \langle \eta^t(t) \rangle &= 0, \\ \langle \eta^r(t) \rangle &= 0. \end{aligned} \quad (9)$$

The strength of these fluctuations balances the dissipation, satisfying the standard fluctuation-dissipation theorem. For the translational noise η^t and rotational noise η^r , the correlations are:

$$\begin{aligned} \langle \eta^t(t) \eta^t(t') \rangle &= 2k_B T \gamma^t \delta(t - t'), \\ \langle \eta^r(t) \eta^r(t') \rangle &= 2k_B T \gamma^r \delta(t - t'). \end{aligned} \quad (10)$$

Here, γ^t and γ^r represent the translational and rotational damping coefficients, respectively.

C. Spontaneous curvature C_0

To account for the behavior of lipids with intrinsic curvature or leaflet asymmetry, we introduce a non-zero spontaneous curvature C_0 . In our model, this is implemented by biasing the tilt and splay interactions to favor a preferred angle between neighboring particles, rather than the parallel alignment we obtain in the absence of spontaneous curvature. For a given value of C_0 , the preferred angle between particles depends on their distance r_{ij} according to $\sin(\frac{\alpha}{2}) = \frac{1}{2}r_{ij}C_0$ (see Supplementary Fig. 12 and Supplementary section A 5). The interaction potentials are modified to penalize deviations from this preferred orientation. The updated energy terms for tilt and splay are given by:

$$U_{\text{tilt}} = \frac{k_{\text{tilt}}}{2} \left[\left(\hat{n}_i \cdot \hat{r} + \frac{1}{2}rC_0 \right)^2 + \left(\hat{n}_j \cdot \hat{r} - \frac{1}{2}rC_0 \right)^2 \right], \quad (11)$$

$$U_{\text{splay}} = \frac{k_{\text{splay}}}{2} \left[\hat{n}_i \cdot \hat{n}_j - 1 + 2 \left(\frac{1}{2}C_0r \right)^2 \right]^2. \quad (12)$$

D. Implementation in LAMMPS

We implemented Langevin dynamics using a combination of the NVE and LANGEVIN fixes in LAMMPS. Together, these commands function as a modified Verlet integrator, incorporating both the random and frictional forces necessary to solve the Langevin equations of motion.

Unless stated otherwise, our simulation parameters are:

- LJ units: $\sigma = 1.0$, $\varepsilon = 1.0$,
- timestep: $\Delta t = 0.01 \tau_{\text{LJ}}$,
- translational damping coefficient: $\gamma_t = 1.0 \tau_{\text{LJ}}^{-1}$,
- rotational damping coefficient: $\gamma_r = 1.6 \sigma^2 \tau_{\text{LJ}}^{-1}$.

We performed benchmarks to test parallelization and scalability of our systems (see Supplementary Fig. 16).

Examples of LAMMPS scripts are publicly available in our Gitlab repository.

III. RESULTS & DISCUSSION

We begin by establishing the feasibility of self-assembly and the conditions under which a membrane is stable, ensuring the system reaches a robust equilibrium configuration capable of maintaining the layer's integrity. Following upon the structural integrity, we characterize the membrane's phase behavior and lipid diffusivity. We use

the results of the diffusivity measurement to map simulation results to physical units, which allows us to directly measure physical quantities. Considering the membrane as a material, we measure its constitutive properties, specifically the area compressibility and bending modulus, which dictate the membrane's energetic response to mechanical stress and thermal fluctuations.

Finally, as example applications, we study the wrapping of a solid particle by the membrane and we simulate the membrane reshaping after an osmotic shock. Fig. 3 shows an overview of our simulation results.

A. Self-assembly

As the first step in the validation of the model, we determined whether our simulated particles can spontaneously assemble into lamellar structures from a disordered state. We initialized the system with a random configuration of $N = 1500$ particles in a cubic box of side length $L = 20\sigma$. This configuration corresponds to a reduced volume fraction of $\phi = NV_p/V_{\text{box}} \approx 0.1$, where $V_p = \frac{1}{6}\pi\sigma^3$ is the volume of a single particle. Particles started forming small patches at intermediate stages ($t = 500 \tau_{\text{LJ}}$), as can be seen in Supplementary Fig. 13. The membrane patches then coalesce into large planar membranes around $t = 2000 \tau_{\text{LJ}}$.

Supplementary Fig. 14 displays representative snapshots of the system at an intermediate stage ($t = 500 \tau_{\text{LJ}}$) across a range of tilt moduli k_{tilt} . Secondary model parameters were held fixed at $k_{\text{splay}} = 1$, $\zeta = 5.0$, $w_c = 2.0\sigma$ and a cutoff radius $r_c = 2.5\sigma$. We find that k_{tilt} is the critical control parameter governing the morphology of the assembled structures. At values below $k_{\text{tilt}} \approx 10.0$, the energetic penalty for director misalignment is too weak to maintain planar order, leading instead to compact, isotropic aggregates. Once k_{tilt} surpasses this threshold, increased orientational stiffness drives these clusters to flatten into membrane-like patches. Unless otherwise noted, k_{tilt} is set to a standard value of 12.0. These patches continue to grow and coalesce into large planar membranes at $t = 2000 \tau_{\text{LJ}}$.

The morphology of growing membrane patches is governed by the competition between the bending energy, which favors a flat geometry (for zero spontaneous curvature $C_0 = 0$), and the line tension, which penalizes the open edges of the patch. Vesiculation occurs when the energetic gain from eliminating the edge exceeds the cost of bending the membrane into a closed shell. To observe this transition, we extended the simulation time to $3500 \tau_{\text{LJ}}$, at which point we observed the spontaneous formation of closed vesicles, see Supplementary Fig. 13. To distinguish between kinetic assembly and thermodynamic stability, we compared these results to the behavior of pre-formed structures. We find that the larger spherical shells described in Sec. B of the Supplementary Material (Fig. 3D) remain structurally intact and stable under identical simulation conditions. This observation

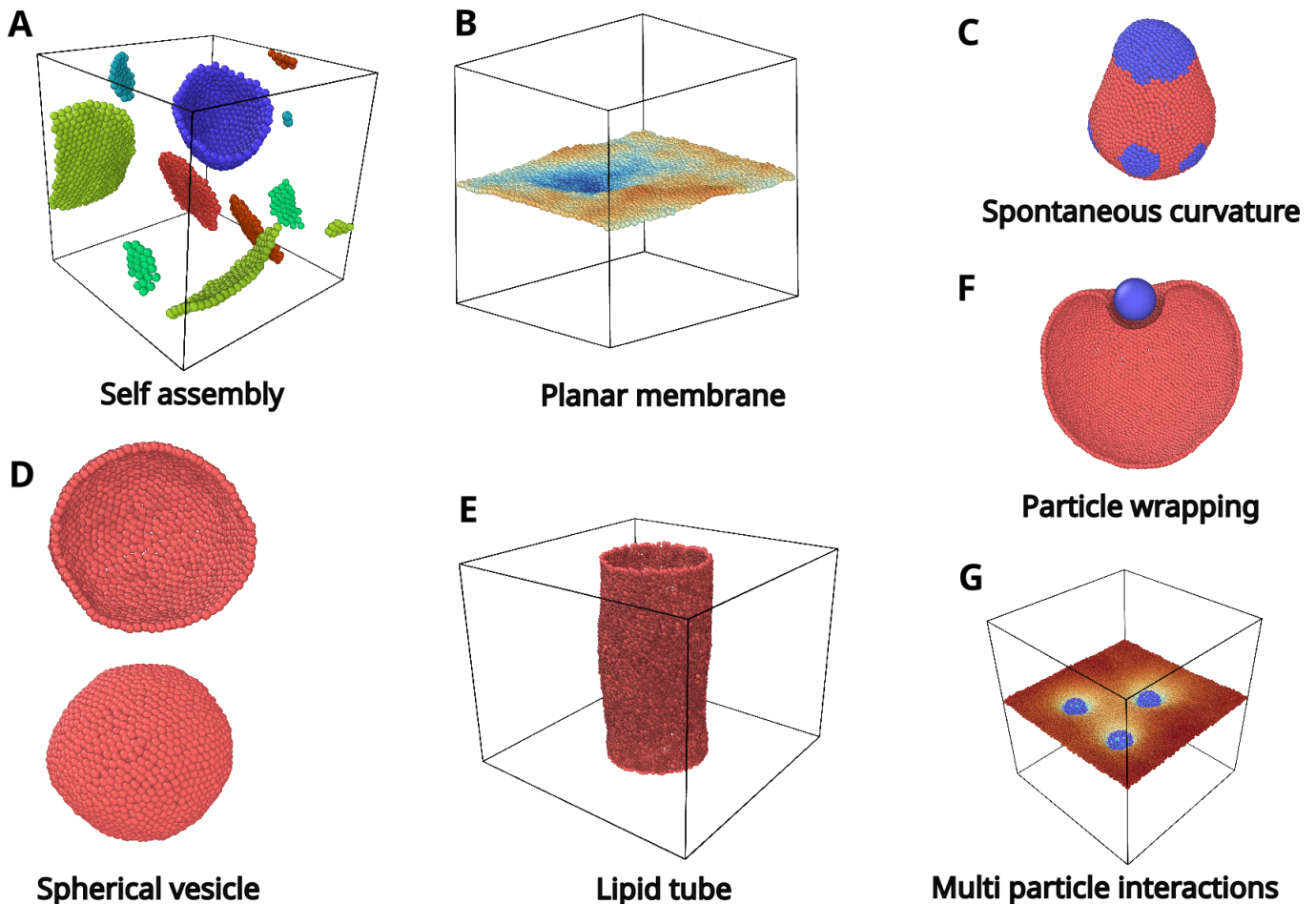


FIG. 3: Overview of simulated lipid systems. (A) Self-assembled patches formed from 1500 randomly placed particles. (B) Planar membrane colored according to z -height. (C) Lipid vesicle composed of zero spontaneous curvature beads (in red) and non-zero spontaneous curvature $C_0 = 0.1\sigma^{-1}$ beads (in blue). (D) Spherical vesicle shown as an xz -cross-section (top) and whole vesicle (bottom). (E) Membrane tube. (F) Cross-section (xz -plane) of a spherical vesicle wrapping a particle. (G) Planar membrane interacting with multiple soft colloidal metaparticles [19]. Initial configurations have been generated following the procedures described in Sec. B of the Supplementary Material.

confirms that the model is capable of maintaining stable vesicular morphologies.

B. Conditions of stability

To test whether our interaction scheme supports a stable planar membrane, we prepared initial configurations by placing particles on a hexagonal lattice with spacing $a = 0.8\sigma$. A lattice of 50×50 sites was used as benchmark size: it is large enough to limit finite-size effects while remaining computationally feasible. Simulations were performed using Langevin dynamics as detailed in Sec. II. We introduced a barostat as well, to ensure that the lateral pressure in the membrane vanished, *i.e.*, $P_{xx} = P_{yy} = 0$, thereby ensuring a tension-

free equilibrium state. Each system was simulated for 5×10^4 steps with time step $\Delta t = 0.01\tau_{LJ}$, which allows the planar membrane to relax from the initial condition. Stability is evaluated by monitoring particle clustering. A simulation is considered stable if, at the end of the run, the majority (more than 99%) of particles belong to a single bigger cluster corresponding to the planar membrane. We tolerated single particle evaporation events, as long as the planar membrane remained intact and continuous. This criterion was checked using a clustering algorithm, the results are shown in Supplementary Fig. 15.

Our parameter sweep yielded the following observations:

- **Interaction cutoff (r_c):** A minimum cutoff of $r_c = 2.5\sigma$ is required to sustain aggregation. Beyond this value, the membrane stability is largely

insensitive to further increases in interaction range.

- **Orientation cutoff (w_c):** This parameter is effectively upper-bounded by r_c . Variations below this bound showed negligible impact on structural stability (see Supplementary Fig. 15) but a significant influence on the mechanical stiffness of the membrane as discussed in section III D 4 below.
- **Tilt modulus (k_{tilt}):** A value of $k_{\text{tilt}} > 10.0$ is strictly necessary to stabilize the planar topology against collapse into isotropic clusters. Above this critical stiffness, the membrane remains robust.
- **Splay modulus (k_{splay}):** Interestingly, the splay constant k_{splay} exhibits significant influence on the stability of the flat membrane. Most of the simulations have been run with a range $0.5 \leq k_{\text{splay}} \leq 1.0$. Values above this range disrupt the stability of the membrane.
- **Attraction slope (ζ):** For low values $\zeta \ll 6.0$ the systems is jammed and solid-like due to the longer range of attraction (see section III D 1).
- **Temperature (T):** Although not an explicit parameter of the force field, the temperature together with ζ acts as the principal driver of phase behavior. At low T we obtain a crystalline or gel-like planar membrane, while increasing T induces a fluid phase, eventually leading to complete sublimation (evaporation) of the bilayer at high T .

The phase diagram (Fig. 4) highlights the effects of ζ and T values leading to distinct gel, liquid, and gas regions.

C. Spontaneous curvature

Fig. 3C depicts a vesicle composed of two bead types: type A (in red) with zero spontaneous curvature ($C_0 = 0$) and type B (in blue) with positive spontaneous curvature ($C_0 = 0.1\sigma^{-1}$). A vesicle consisting of an initially random mixture of type A and type B particles undergoes phase separation and changes its shape to minimize the bending and mixing energy. While not the primary focus of this study, this example demonstrates how spontaneous curvature and different lipid types can be incorporated easily into our framework.

D. Membrane characterization

Following the stability assessment of the membrane layer, we characterized its fundamental physical properties and their dependence on system parameters. We focused on key metrics standard in computational membrane models: the phase diagram, lipid lateral diffusivity,

area compressibility, and bending modulus. We evaluated these properties using the previously described system, consisting of a planar square membrane of 2500 particles under periodic boundary conditions and run for 10^5 steps.

1. Phase diagram and lipid diffusivity

To characterize the physical state of the membrane, we analyzed the scaling behavior of the lipid Mean Squared Displacement (MSD), characterized as $\text{MSD}(t) \propto t^\alpha$. By plotting the exponent α as a heat map in the (T, ζ) parameter space (Fig. 4), we can easily identify three distinct dynamical regimes. The system exhibits a clear separation between a sub-diffusive solid/gel phase ($\alpha \ll 1$), a diffusive liquid fluid phase ($\alpha \approx 1$), and a super-diffusive gas-like regime ($\alpha \gg 1$) corresponding to membrane disintegration.

The phase behavior is primarily governed by the temperature T and the interaction parameter ζ , which controls the attractive slope of the inter-particle potential. An increase of ζ at higher temperature T leads to a transition to the gas phase. This counter intuitive behaviour can be explained by the fact that a higher value of ζ not only gives rise to stronger restoring forces but also effectively reduces the attractive range as well. Secondary model parameters were held fixed at $k_{\text{tilt}} = 12$, $k_{\text{splay}} = 12$, $w_c = 1.7\sigma$ and a cutoff radius $r_c = 2.5\sigma$.

Following the phase analysis, we quantified the lipid dynamics within the stable membrane regimes. We determined the lateral diffusion coefficient D by fitting the linear regime of the MSD to the relation for two-dimensional diffusion, $\text{MSD} = 4Dt$. Data points corresponding to the gas phase were excluded from this analysis as the diffusive model is not applicable to unbound particles. Fig. 5 shows the dependence of lipid diffusivity on T and ζ .

2. Real world unit mapping

To relate the simulation parameters to physical scales, we map the model units σ and τ_{LJ} to the properties of a typical phospholipid membrane. Equating our particle size σ to the lipid bilayer thickness (5 nm) and given that a single lipid molecule occupies an area of 0.5 nm^2 , it follows that each particle in our membrane model represents ≈ 300 lipids (150 in each leaflet).

The time scale is determined using the lipid diffusion constant. Given a characteristic experimentally measured lateral diffusion constant $D \approx 1 \mu\text{m}^2/\text{s}$ [20] and a measured simulation diffusion constant $D_{\text{sim}} = 0.25\sigma^2/\tau_{\text{LJ}}$, the simulation time unit maps to $\tau_{\text{LJ}} \approx 6.25 \mu\text{s}$.

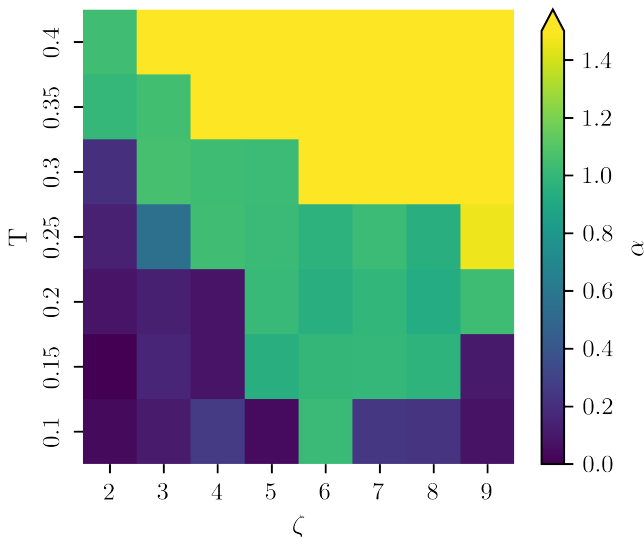


FIG. 4: Dynamical phase diagram of the membrane model in the (T, ζ) parameter space. The color map represents the scaling exponent α obtained from the power-law fit of the lipid Mean Squared Displacement ($\text{MSD} \propto t^\alpha$). We identify three distinct regimes: a sub-diffusive solid/gel phase ($\alpha \ll 1$), a diffusive fluid phase ($\alpha \approx 1$), and a super-diffusive gas-like regime ($\alpha \gg 1$) corresponding to membrane disintegration.

Fixed model parameters: $N = 2500$, $k_{\text{tilt}} = 12$, $k_{\text{splay}} = 12$, $w_c = 1.7\sigma$ and $r_c = 2.5\sigma$.

3. Area compressibility modulus

The area compressibility modulus, K_A , quantifies the membrane's resistance to isotropic expansion. This parameter is determined by analyzing the stress-strain response of the system under lateral tension. In our simulations, we subjected a planar membrane (2500 particles) to equibiaxial stretching ($\gamma_{xx} = \gamma_{yy}$) across the xy -plane. We monitored the resulting surface tension, Σ , as a function of the projected area until the onset of mechanical failure, defined by the formation of a membrane pore.

The modulus K_A is derived from Hooke's law for elastic membranes in the low-strain regime:

$$\Sigma = K_A \frac{A - A_0}{A_0} \quad (13)$$

where A is the projected area under tension, A_0 is the equilibrium area at zero tension, and the term $(A - A_0)/A_0$ represents the area strain α . By plotting the applied tension Σ against the area strain, we can obtain K_A from the slope of the linear fit (Fig. 6A).

The area compressibility modulus K_A was extracted from the linear regime of the tension-strain curves prior to failure. Our analysis reveals distinct dependencies of K_A on the thermodynamic phase of the system (gel, liquid, or gas). By comparing the compressibility data in Fig. 6 with the phase diagram in Fig. 4, we observe a

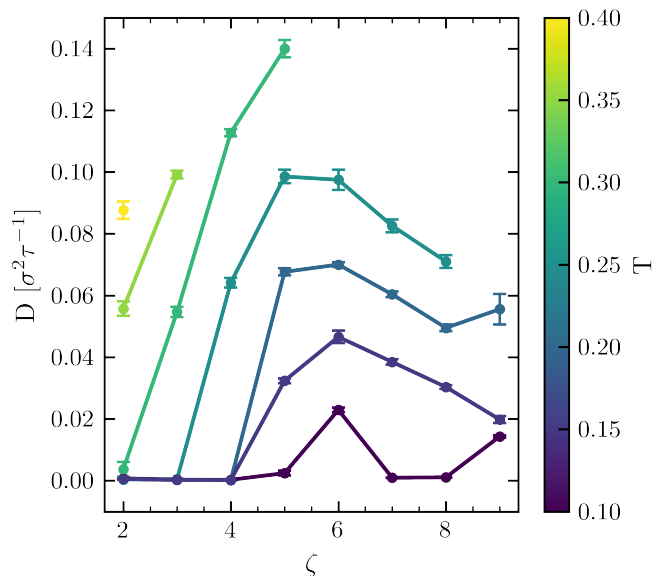


FIG. 5: Lateral diffusion coefficient D of membrane lipids as a function of temperature T and interaction parameter ζ , from the same simulations as used for Fig. 4. D was calculated by fitting the MSD to $\text{MSD} = 4Dt$ in the linear regime. Points of the dataset corresponding to a system in the gas phase have been excluded from the plot. Errorbars are standard deviations over 3 independent replicas.

significant mechanical response at the phase boundaries. Specifically, a sharp decrease in K_A occurs at the gel-to-liquid transition, signaling the loss of long-range translational order. As anticipated, the primary parameters influencing K_A are those governing the phase behavior: the temperature T and the attractive slope parameter ζ . Both parameters strongly modulate K_A by driving the phase transitions. High K_A values are characteristic of the solid-like (gel) phase, whereas a marked reduction is observed in the fluid-like phase. By tuning these interactions, the model can be calibrated to reproduce physiological compressibility moduli, typically on the order of $K_A \approx 20 k_B T / \sigma^2$ [21].

4. Fluctuation spectrum and bending modulus

According to continuum membrane theory, the height fluctuation spectrum in the tensionless regime is described by the Helfrich expression [22]:

$$\langle |h_q|^2 \rangle = \frac{1}{L^2} \frac{k_B T}{\kappa q^4}, \quad (14)$$

where $k_B T$ is the thermal energy, L is the lateral box size, κ is the bending modulus, and q is the magnitude of the wave vector. To compute the spectrum and perform the fitting procedure, we adopted the analysis framework established by Muñoz-Basagoiti *et al.* [23], inspired by the

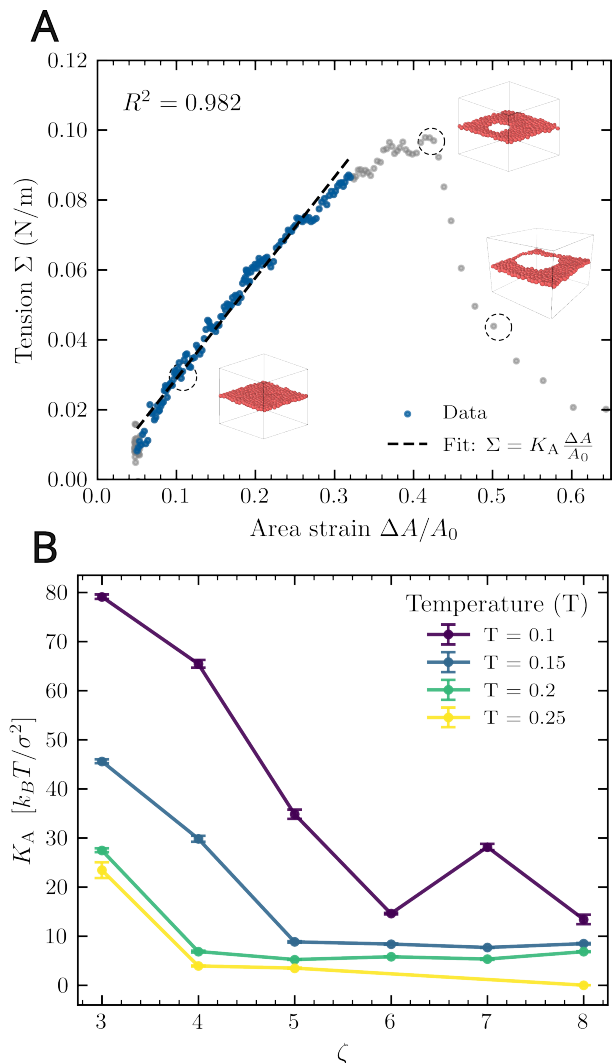


FIG. 6: (A) Representative plot of tension Σ versus area strain $(A - A_0)/A_0$. The compressibility modulus K_A is determined from the slope of the linear regime. Rupture occurs at a strain of ≈ 0.4 . The parameters for this simulation are $N = 400$, $k_{\text{tilt}} = 12$, $k_{\text{splay}} = 12$, $\zeta = 5.0$, $w_c = 1.7\sigma$, $T = 0.3$. (B) Compressibility modulus K_A as a function of temperature T and slope parameter ζ . The sharp decrease in K_A corresponds to the transition from a solid-like to a fluid-like phase. The parameters for this dataset are $N = 2500$, $k_{\text{tilt}} = 12$, $k_{\text{splay}} = 12$, $w_c = 1.7\sigma$

error analysis protocols in [24]. We adapted their implementation—originally designed for the Cooke-Deserno three-bead model—to accommodate the specific geometry of our membrane model. All reported values for κ satisfy the goodness-of-fit criterion $Q > 10^{-4}$, as recommended in Ref. [24]. The membrane was simulated following the stability protocols described in Section III B. System equilibration was verified by monitoring the convergence of the lateral box area ($L_x \times L_y$) to a steady-state plateau. To ensure statistically independent sam-

pling, we calculated the time autocorrelation function for the Fourier modes. The decorrelation time for the lowest- q mode was found to be approximately $1000 \tau_{LJ}$, which was subsequently used as the sampling interval. A total of 250 uncorrelated snapshots were used to compute the power spectrum. As illustrated in Fig. 7, the fluctuation spectrum of the simulated membrane exhibits the characteristic q^{-4} scaling expected for a tensionless interface. The bending modulus κ was extracted by fitting the numerical data to Eq. 14. As shown in Figs. 7 and 8, the effective membrane stiffness is primarily governed by the orientational cutoff w_c and the tilt modulus k_{tilt} , while the splay modulus k_{splay} has only a minor effect. We confirmed that κ is independent of both the coupling parameter ζ and the cutoff radius r_{cut} . Physically, increasing w_c stiffens the membrane by incorporating a greater number of neighbors into the local orientation penalty. A similar stiffening effect is observed when increasing k_{tilt} . By tuning these parameters, the model accurately reproduces physiological bending moduli in the range of $10\text{--}30k_B T$ [21, 25].

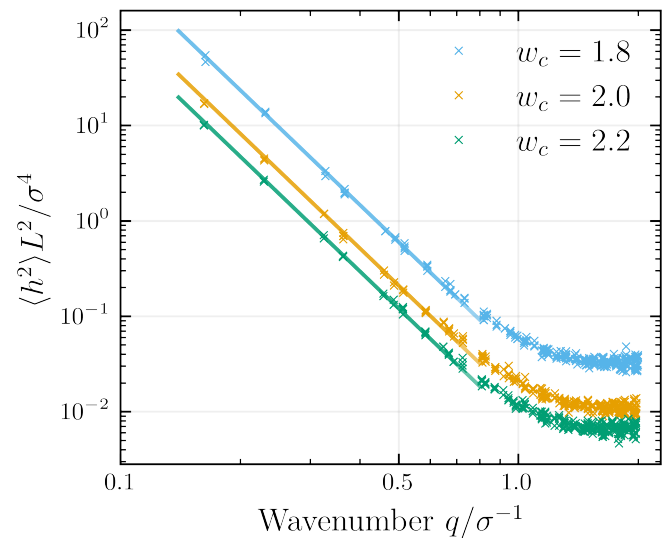


FIG. 7: Power spectrum of membrane height fluctuations. The mean squared amplitude $\langle |h_q|^2 \rangle$ is plotted against the wave number q . The simulation data exhibits a clear q^{-4} scaling behavior, consistent with the theoretical prediction for a tensionless membrane. This confirms that the system is in a zero-surface-tension state ($P_{xx} = P_{yy} = 0$), where fluctuations are governed solely by bending rigidity.

E. Particle wrapping

To demonstrate the applicability of our model, we investigated the adhesive interaction between a colloidal particle and a fluid membrane, corresponding to frequently used adhesion assays in biophysical studies [26]

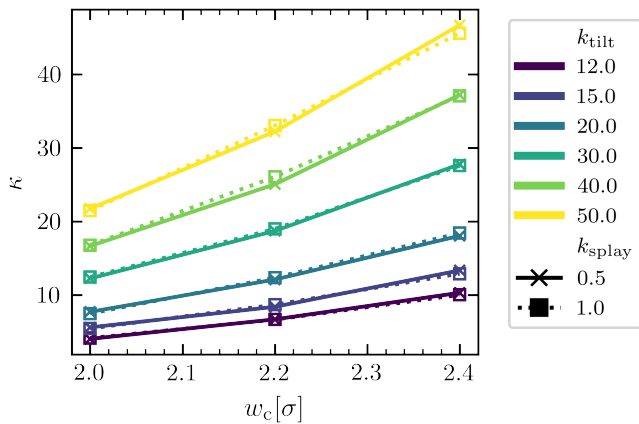


FIG. 8: Dependence of the bending modulus κ on model parameters. The membrane rigidity increases monotonically with the orientational cutoff w_c and the tilt modulus k_{tilt} . In contrast, the splay modulus k_{splay} has a negligible impact on the overall bending modulus.

and as a simple model for endocytosis [27]. We compared two distinct configurations: a spherical vesicle of radius $R_{\text{ves}} \approx 29\sigma$ (12500 particles) and a planar periodic membrane patch of size $L = 50\sigma$ (2500 particles). Membrane model parameters are set to ensure a soft and diffusive lipid bilayer: $k_{\text{tilt}} = 12$, $k_{\text{splay}} = 12$, $\zeta = 5.0$, $w_c = 1.6\sigma$ and a cutoff radius $r_c = 2.5\sigma$. The colloid is modeled as a spherical particle which interacts with the membrane through a 12-6 Lennard-Jones potential with a minimum at $\sigma_{\text{mix}} = (\sigma + \sigma_{\text{coll}})/2$ and a varying attraction strength $\varepsilon_{\text{coll}}$. The potential was truncated at a cutoff $r_{\text{coll}} = \sigma_{\text{mix}} + 2\sigma$. Simulations were performed using Langevin dynamics as detailed in Sec. II. For the planar system, we utilized a barostat to maintain zero lateral tension, ensuring that the wrapping process was governed primarily by the interplay of adhesion and bending elasticity rather than membrane stretching. In the initial configuration of the simulation we placed the colloidal particle at a distance $d = r_{\text{coll}} + 2\sigma$ from an equilibrated membrane and gave it a small velocity directed towards the membrane. Each system was simulated for 5×10^5 steps with time step $\Delta t = 0.01\tau_{\text{LJ}}$, which allows it to reach a steady state for the process.

We determined the particle wrapping fraction χ by identifying the membrane beads which are within the interaction radius and fitting a circular arc to their coordinates on the midplane. This geometric fit allows for a robust estimation of the extent of the contact zone. The data presented in Fig. 9 represent averages over the final 15 frames of each simulation.

We observed consistent behavior across both the vesicle and the planar patch geometries: the wrapping fraction increases monotonically with the interaction strength $\varepsilon_{\text{coll}}$ and decreases with the colloidal radius R_{coll} . While a larger radius increases the possible contact area, it also imposes a higher energetic cost due to the

bending required to follow the particle's curvature. These results are in qualitative agreement with theoretical predictions for the wrapping of rigid spheres by fluid membranes, where the transition from partial to full wrapping is determined by the balance between adhesive energy gain and the bending energy penalty.

F. Volume control protocol

To demonstrate the model's extensibility to realistic experimental conditions, such as osmotic shock, we implemented a volume control protocol based on the methodology established by [12, 13]. The protocol entails adding explicit solvent particles inside and outside a vesicle creating an effective pressure. This approach allows us to investigate how the vesicle adapts its morphology under varying pressure differences; a description of the simulation procedure is provided in Supplementary Materials Section A.

To characterize the resulting morphologies, we calculated the reduced volume ν , a dimensionless parameter that measures the deviation of the vesicle from a spherical shape:

$$\nu = \frac{V_{\text{ve}}}{\frac{4}{3}\pi R_{\text{ve}}^3}.$$

Here, R_{ve} represents the equivalent radius of a sphere with the same surface area A_{ve} as the vesicle, defined as:

$$R_{\text{ve}} = \sqrt{\frac{A_{\text{ve}}}{4\pi}}$$

The relationship between the external density, the internal/external concentration ratio, and the resulting vesicle shape is summarized in Fig. 10. The resulting shapes qualitatively agree with numerical solutions of the axisymmetric vesicle shape equation derived from the Helfrich energy [28, 29].

IV. CONCLUSION

We have developed an efficient and pragmatic particle based model for simulating lipid bilayer membranes, based on a conceptually simple additive potential combining isotropic and orientational contributions. We have shown that with this model, we can recover essential membrane properties such as spontaneous vesiculation, the correct scaling of the fluctuation spectrum, and biologically relevant bending and compressibility moduli. The model can be easily extended to include multiple lipid types and spontaneous curvature effects. We can also include an effective osmotic pressure to control the membrane's surface-to-volume ratio. We have demonstrated a possible application of this model to colloidal particle wrapping.

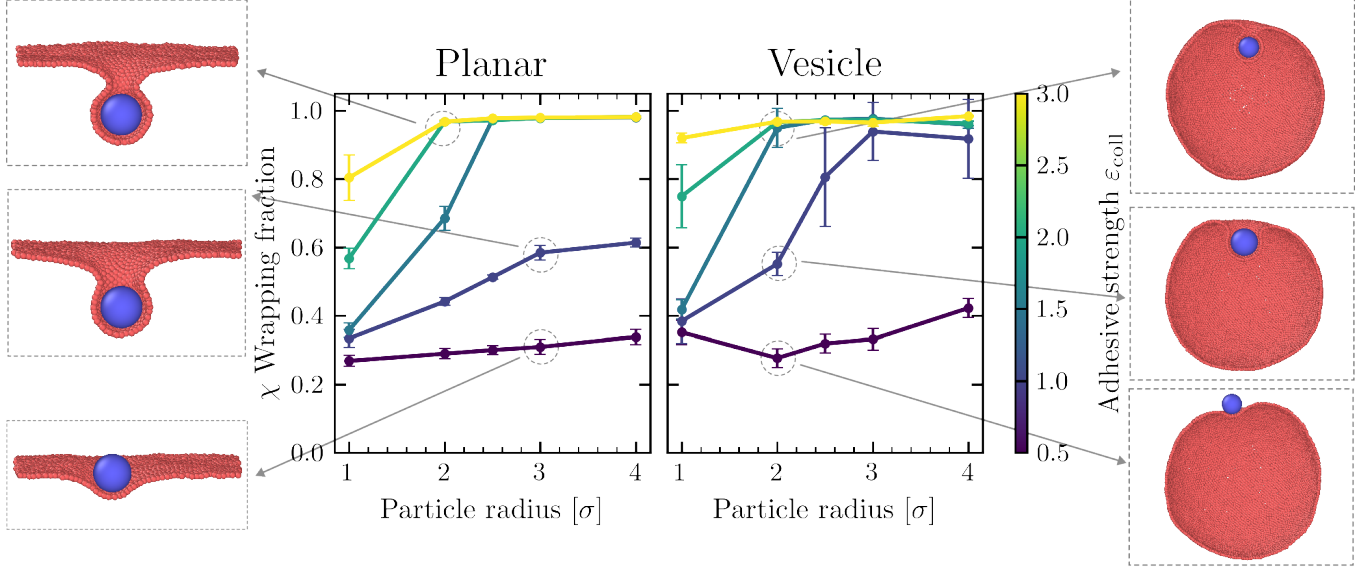


FIG. 9: Wrapping fraction χ of the colloidal particle as a function of attraction strength $\varepsilon_{\text{coll}}$ (indicated in the colorbar) and particle radius r_{coll} . (left) Interaction with a planar periodic membrane patch ($L = 50\sigma$). (right) Interaction with a spherical vesicle ($R_{\text{ves}} \approx 29\sigma$). In both plots, error bars represent the standard deviation of the last 15 simulation frames.

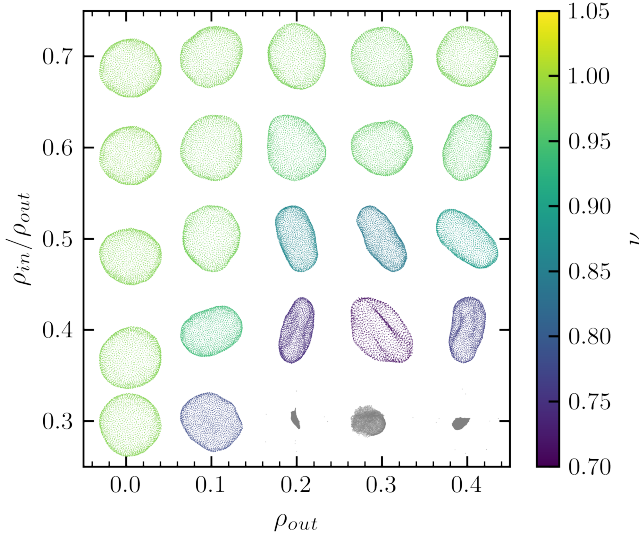


FIG. 10: Phase diagram of vesicle morphologies as a function of outer particles density (x-axis) and the internal/external density ratio (y-axis). The vesicles are color-coded according to the reduced volume ν , illustrating the transition from spherical to deflated states. Burst or unstable vesicles are colored in grey.

Operating at the mesoscopic level, our model can reach length and timescales relevant for cellular processes, including cell motility, cell growth and cell division. We can further extend the model to include interactions with

cytoskeletal elements and membrane-associated proteins, and adhesion between membranes. As such, it complements and bridges between existing molecular-scale models and continuum models.

AUTHOR CONTRIBUTIONS

PS and TI conceived the original idea and developed the theoretical framework. PS designed and performed the simulations, analyzed the data, and wrote the initial manuscript. SM and TI acquired funding, supervised, provided critical feedback, and helped shape the final version of the manuscript.

ACKNOWLEDGMENTS

We thank Felix Frey and Adam Prada for helpful discussions.

This research is supported by the ‘BaSyC - Building a Synthetic Cell’ Gravitation grant (024.003.019) of the Netherlands Ministry of Education, Culture and Science (OCW) and the Netherlands Organisation for Scientific Research (NWO).

Appendix A: Model description

1. Useful math relations

We first establish the decomposition of a vector \vec{n} into components parallel and perpendicular to the radial unit vector \hat{r} :

$$\vec{n} = n^{\parallel} \hat{r} + n^{\perp} \hat{r}^{\perp} = [(\vec{n} \cdot \hat{r}) \hat{r}] + [\vec{n} - (\vec{n} \cdot \hat{r}) \hat{r}].$$

Doing so allows us to define the perpendicular projection operator, represented by the matrix $\mathbf{P}_{\vec{v}^{\perp}}$. This matrix acts on a vector \vec{u} to isolate its transverse component relative to a reference vector \vec{v} :

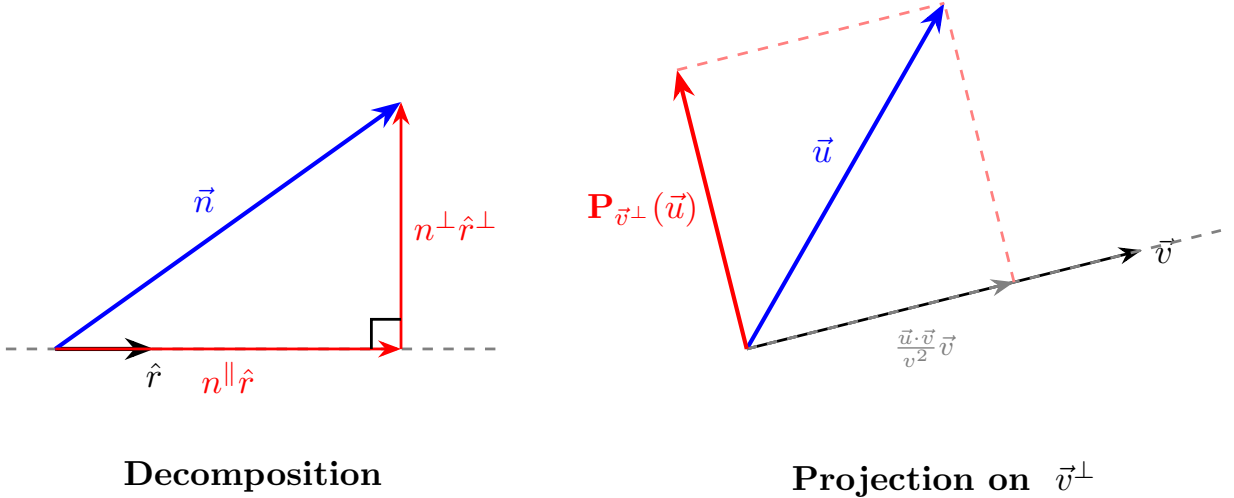
$$\mathbf{P}_{\vec{v}^{\perp}}(\vec{u}) = \vec{u} - \frac{\vec{u} \cdot \vec{v}}{v^2} \vec{v} = \left[\mathbf{I} - \frac{\vec{v} \otimes \vec{v}}{v^2} \right] \vec{u}. \quad (\text{A1})$$

We can rewrite the gradient acting on a vector field in terms of the projection operator:

$$\vec{\nabla} \hat{r} = \frac{\partial \hat{r}}{\partial \vec{r}} = \frac{1}{r} \left(\mathbf{I} - \frac{\vec{r} \otimes \vec{r}}{r^2} \right) = \frac{1}{r} \mathbf{P}_{\hat{r}^{\perp}}.$$

This operator-based approach can be extended to scalar fields U that depend on the orientation \hat{r} :

$$\vec{\nabla} U = \frac{\partial U}{\partial \vec{r}} = \frac{\partial \hat{r}}{\partial \vec{r}} \cdot \frac{\partial U}{\partial \hat{r}} = \frac{1}{r} \left(\mathbf{I} - \frac{\vec{r} \otimes \vec{r}}{r^2} \right) \frac{\partial U}{\partial \hat{r}} = \frac{1}{r} \mathbf{P}_{\hat{r}^{\perp}} \left(\frac{\partial U}{\partial \hat{r}} \right).$$



2. Model definition

Let $\vec{r}_{ij} = \vec{r}_i - \vec{r}_j$ be the separation vector between particle i and particle j , with its magnitude defined as $r = |\vec{r}_{ij}|$. The unit vector \hat{r} is defined as the normalized direction pointing from particle j to particle i :

$$\hat{r} = \frac{\vec{r}_i - \vec{r}_j}{r}.$$

The total energy of our system is given by the sum over the isotropic and the orientational terms, the latter of which are modulated by a distance-dependent weighting function (see Eq. 1 in the main text):

$$H = U_{\text{rep}} + U_{\text{attr}} + w(r) [U_{\text{tilt}} + U_{\text{splay}}].$$

a. *Weighting function*

a. *Force derivation in presence of weighting function* All orientational potentials in this model are scaled by a radial weighting function $w(r)$. To derive the total force, we apply the chain rule for the derivative with respect to \vec{r} :

$$\begin{aligned}\vec{F}_{\text{tot}} &= -\nabla_{\vec{r}}[U(\hat{r})w(r)] = -w(r)\frac{\partial U(\hat{r})}{\partial \hat{r}}\frac{\partial \hat{r}}{\partial \vec{r}} - U(\hat{r})\frac{\partial w(r)}{\partial r}\frac{\partial r}{\partial \vec{r}} \\ &= w(r)\vec{F} - U(\hat{r})w'(r)\hat{r}.\end{aligned}\tag{A2}$$

The first term in equation (A2) is the force due to the potential $U(\hat{r})$ weighted by $w(r)$, without changing direction. The second term is proportional to the interaction energy and to the derivative of the weighting function.

b. *Torque derivation in presence of weighting function* The torques are simpler because for them the weighting function is just a rescaling:

$$\vec{\tau}_{\text{tot}} = -\nabla_{\hat{n}}[U(\hat{r})w(r)] = -w(r)\frac{\partial U(\hat{r})}{\partial \hat{n}} = -w(r)\vec{\tau}.$$

c. *Functional form of the weighting function $w(r)$* We have chosen the functional form for our weighting function $w(r)$ to interpolate smoothly between 1 at $r = 0$ and 0 at the cutoff distance $r = w_c$. The derivative of $w(r)$ vanishes at both $r = 0$ and $r = w_c$, ensuring no jump in force or torque as a particle comes within range.

$$w(r) = \begin{cases} \exp\left(\frac{(r/r_{\text{ga}})^2}{(r/w_c)^n - 1}\right), & r \leq w_c, \\ 0, & r \geq w_c, \end{cases}\tag{A3}$$

typically with $n = 4$ and $r_{\text{ga}} = 1.5\sigma$. The freely adjustable parameter w_c is used to set the effective range of orientational interactions.

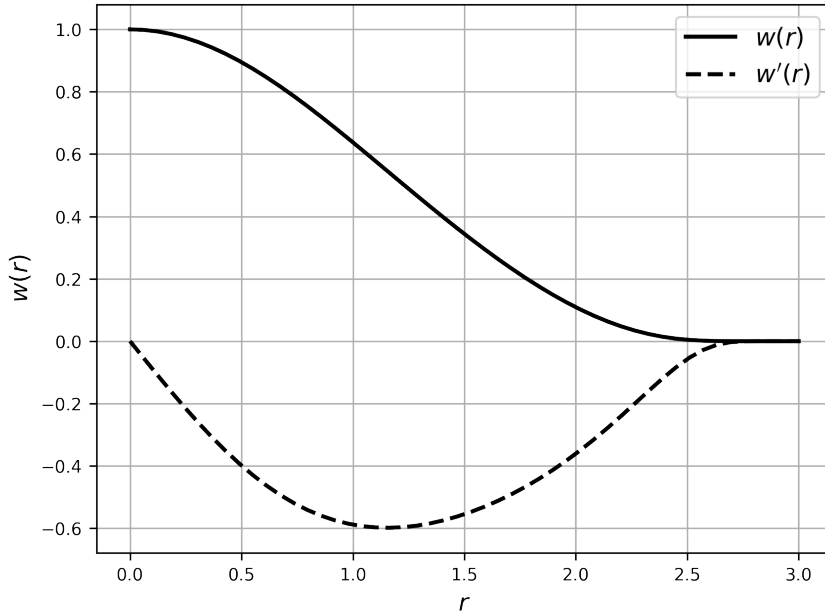


FIG. 11: Plot of weighting function $w(r)$ used in the membrane model.

3. Forces

a. Isotropic potential

For the forces due to the isotropic potential, we obtain:

$$\begin{aligned}\vec{F} &= -\nabla U(r) = -\frac{\partial U}{\partial \vec{r}} = -\frac{\partial U}{\partial r} \frac{\partial r}{\partial \vec{r}} = -\frac{\partial U}{\partial r} \frac{\vec{r}}{r} = -\frac{\partial U}{\partial r} \hat{r}, \\ U_{\text{rep}}(r) &= \epsilon \left[\left(\frac{r_{\text{min}}}{r} \right)^4 - 2 \left(\frac{r_{\text{min}}}{r} \right)^2 \right], \quad r \leq r_{\text{min}}, \\ \vec{F}_{\text{rep}}(r) &= \frac{4\epsilon}{r} \left[\left(\frac{r_{\text{min}}}{r} \right)^4 - \left(\frac{r_{\text{min}}}{r} \right)^2 \right] \hat{r}, \quad r \leq r_{\text{min}}, \\ U_{\text{attr}}(r) &= \begin{cases} -\epsilon \cos^2 \zeta \left(\frac{\pi(r - r_{\text{min}})}{2(r_c - r_{\text{min}})} \right), & r_{\text{min}} < r < r_c, \\ 0, & r \geq r_c, \end{cases} \\ \vec{F}_{\text{attr}}(r) &= \epsilon \frac{\pi}{r_c - r_{\text{min}}} \zeta \cos^{2\zeta-1} \left(\frac{\pi(r - r_{\text{min}})}{2(r_c - r_{\text{min}})} \right) \sin \left(\frac{\pi(r - r_{\text{min}})}{2(r_c - r_{\text{min}})} \right)\end{aligned}$$

b. Tilt

$$\begin{aligned}U_{\text{tilt}} &= \frac{k_{\text{tilt}}}{2} [(\hat{n}_i \cdot \hat{r})^2 + (\hat{n}_j \cdot \hat{r})^2], \\ \vec{\nabla} U &= \frac{\partial U}{\partial \vec{r}} = \frac{\partial U}{\partial \hat{r}} \frac{\partial \hat{r}}{\partial \vec{r}} = \frac{1}{r} \frac{\partial U}{\partial \hat{r}} \left(\mathbf{I} - \frac{\vec{r} \otimes \vec{r}}{r^2} \right) = \frac{1}{r} \frac{\partial U}{\partial \hat{r}} \mathbf{P}_{\vec{r}^\perp}, \\ \vec{F} &= -\nabla U_{\text{tilt}} = -\frac{\partial}{\partial \vec{r}} U_{\text{tilt}}(\hat{r} \cdot \hat{n}_i, \hat{r} \cdot \hat{n}_j) = -\frac{\partial U_{\text{tilt}}}{\partial \hat{r}} \frac{\partial \hat{r}}{\partial \vec{r}} = -\frac{\partial U_{\text{tilt}}}{\partial \hat{r}} \frac{1}{r} \mathbf{P}_{\vec{r}^\perp},\end{aligned}$$

using Eq. (A1).

a. Force on particle i

$$\begin{aligned}\vec{F}_i &= -\frac{k_{\text{tilt}}}{2} [2(\hat{n}_i \cdot \hat{r})\hat{n}_i + 2(\hat{n}_j \cdot \hat{r})\hat{n}_j] \frac{\partial \hat{r}}{\partial \vec{r}} \\ &= -\frac{k_{\text{tilt}}}{2} \left[2(\hat{n}_i \cdot \hat{r}) \frac{1}{r} (\hat{n}_i - (\hat{n}_i \cdot \hat{r})\hat{r}) + 2(\hat{n}_j \cdot \hat{r}) \frac{1}{r} (\hat{n}_j - (\hat{n}_j \cdot \hat{r})\hat{r}) \right] \\ &= -\frac{k_{\text{tilt}}}{2} \left[2 \frac{(\hat{n}_i \cdot \hat{r})}{r} \vec{n}_i^\perp + 2 \frac{(\hat{n}_j \cdot \hat{r})}{r} \vec{n}_j^\perp \right],\end{aligned}$$

where $\vec{n}_i^\perp = \hat{n}_i - (\hat{n}_i \cdot \hat{r})\hat{r}$ is the projection of \hat{n}_i onto the plane perpendicular to \hat{r} .

b. Force on particle j Substituting the flipped unit vector into the expression for \vec{F}_i , we find:

$$\vec{F}_j = +\frac{k_{\text{tilt}}}{r} [(\hat{n}_i \cdot \hat{r})\vec{n}_i^\perp + (\hat{n}_j \cdot \hat{r})\vec{n}_j^\perp].$$

This yields the relation $\vec{F}_j = -\vec{F}_i$, confirming that the internal forces of the pair interaction satisfy Newton's third law and conserve the total linear momentum of the system.

c. Splay

$$U_{\text{splay}} = \frac{k_{\text{splay}}}{2} (\hat{n}_i \cdot \hat{n}_j - 1)^2. \quad (\text{A4})$$

The splay term is not generating any force onto the interacting pair.

4. Torques

Following the derivation from Allen [30], the torques can be expressed as:

$$\begin{aligned}\vec{\tau}_i &= \frac{\partial U}{\partial(\hat{n}_i \cdot \hat{r})}(\hat{r} \times \hat{n}_i) - \frac{\partial U}{\partial(\hat{n}_i \cdot \hat{n}_j)}(\hat{n}_i \times \hat{n}_j) \\ \vec{\tau}_j &= \frac{\partial U}{\partial(\hat{n}_j \cdot \hat{r})}(\hat{r} \times \hat{n}_j) + \frac{\partial U}{\partial(\hat{n}_i \cdot \hat{n}_j)}(\hat{n}_i \times \hat{n}_j)\end{aligned}$$

a. Isotropic potential

The isotropic potential term is not generating any torque onto the interacting pair.

b. Tilt

$$\begin{aligned}\vec{\tau}_i &= \frac{k_{\text{tilt}}}{2} 2(\hat{n}_i \cdot \hat{r})(\hat{r} \times \hat{n}_i) = \frac{k_{\text{tilt}}}{2} 2(\hat{n}_i \cdot \hat{r})(\hat{r} \times \hat{n}_i), \\ \vec{\tau}_j &= \frac{k_{\text{tilt}}}{2} 2(\hat{n}_j \cdot -\hat{r})(-\hat{r} \times \hat{n}_j) = \frac{k_{\text{tilt}}}{2} 2(\hat{n}_j \cdot \hat{r})(\hat{r} \times \hat{n}_j).\end{aligned}$$

c. Splay

$$\begin{aligned}\tau_i &= -\frac{k_{\text{splay}}}{2} (-2)(\hat{n}_i \cdot \hat{n}_j - 1)(\hat{n}_i \times \hat{n}_j) = k_{\text{splay}}(\hat{n}_i \cdot \hat{n}_j - 1)(\hat{n}_i \times \hat{n}_j), \\ \tau_j &= +\frac{k_{\text{splay}}}{2} (-2)(\hat{n}_i \cdot \hat{n}_j - 1)(\hat{n}_i \times \hat{n}_j) = -k_{\text{splay}}(\hat{n}_i \cdot \hat{n}_j - 1)(\hat{n}_i \times \hat{n}_j).\end{aligned}$$

5. General case with spontaneous curvature

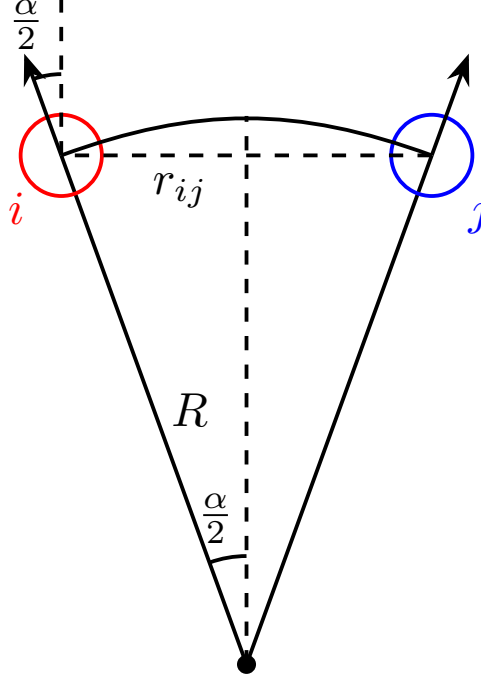


FIG. 12: Schematic for spontaneous curvature geometry.

If we include a non-zero spontaneous curvature as described in section II C, the tilt and splay energies are modified to:

$$\begin{aligned}
 U_{\text{tilt}} &= \frac{k_{\text{tilt}}}{2} [(\hat{n}_i \cdot \hat{r} + \sin(\alpha/2))^2 + (\hat{n}_j \cdot \hat{r} - \sin(\alpha/2))^2] \\
 &= \frac{k_{\text{tilt}}}{2} \left[\left(\hat{n}_i \cdot \hat{r} + \frac{1}{2} r C_0 \right)^2 + \left(\hat{n}_j \cdot \hat{r} - \frac{1}{2} r C_0 \right)^2 \right], \\
 U_{\text{splay}} &= \frac{k_{\text{splay}}}{2} (\hat{n}_i \cdot \hat{n}_j - \cos \alpha)^2 \\
 &= \frac{k_{\text{splay}}}{2} \left[\hat{n}_i \cdot \hat{n}_j - 1 + 2 \left(\frac{1}{2} C_0 r \right)^2 \right]^2.
 \end{aligned}$$

The preferred angle α is coupled to the distance r between the particles according to $\sin \frac{\alpha}{2} = \frac{1}{2} r C_0$, where C_0 is the spontaneous curvature. In the limit where the spontaneous curvature vanishes ($C_0 \rightarrow 0$) the simplified form is recovered.

a. *Tilt*

Force on particle i :

$$\begin{aligned}\vec{F}_i &= \frac{k_{\text{tilt}}}{r} \left[(\hat{n}_i \cdot \hat{r} + \frac{1}{2}rC_0)(\hat{n}_i - (\hat{n}_i \cdot \hat{r})\hat{r}) + (\hat{n}_j \cdot \hat{r} - \frac{1}{2}rC_0)(\hat{n}_j - (\hat{n}_j \cdot \hat{r})\hat{r}) \right] \\ &= \frac{k_{\text{tilt}}}{r} \left[(\hat{n}_i \cdot \hat{r} + \frac{1}{2}rC_0)\vec{n}_i^\perp + (\hat{n}_j \cdot \hat{r} - \frac{1}{2}rC_0)\vec{n}_j^\perp \right].\end{aligned}$$

Torque on particle i :

$$\vec{\tau}_i = -k_{\text{tilt}} \left(\hat{n}_i \cdot \hat{r} + \frac{1}{2}rC_0 \right) (\hat{r} \times \hat{n}_i).$$

b. *Splay*

Unlike the case of zero spontaneous curvature, the generalized splay term results in a force acting onto the interacting particles:

$$\vec{F}_i = -k_{\text{splay}}C_0^2r \left[\hat{n}_i \cdot \hat{n}_j - 1 + 2 \left(\frac{1}{2}rC_0 \right)^2 \right] \hat{r}$$

Torque on particle i :

$$\vec{\tau}_i = -k_{\text{splay}} \left[\hat{n}_i \cdot \hat{n}_j - 1 + \frac{1}{2}(rC_0)^2 \right] (\hat{n}_i \times \hat{n}_j).$$

Appendix B: System preparation

1. Planar membrane initial configuration

As already mentioned in section III B of the main text, we have used a two-dimensional hexagonal packing as the template for the initial configuration. The distance between adjacent hexagonal cells is 0.8σ . For these simulations we use periodic boundary conditions, so edge particles need to be close enough to the box edge to interact with their periodic neighbors to conserve plane continuity.

2. Spherical vesicle initial configuration

To initialize the vesicle, we used the icosphere package [31] to generate a triangular mesh of a sphere. This method takes an icosahedron as a starting point, and then iteratively subdivides its triangles, creating a mesh of the sphere. We then place single particles with outward orientation at the barycenter of each triangle. An important final step is to rescale the neighbors distance to around 0.8σ .

3. Lipid tube initial configuration

To generate a lipid tube, we extend the setup used for the planar membrane by mapping the hexagonal lattice onto a cylindrical geometry. The initial configuration is defined by a radius R and a total length L along the longitudinal axis, typically aligned with the z -direction of the simulation box. We also check that beads at the top and bottom boundaries can interact smoothly under periodic boundary conditions. Similar to the planar case, the equilibrium distance between nearest neighbors is scaled to approximately 0.8σ .

4. Volume control configuration

To simulate an osmotic shock and achieve precise control over the vesicle volume, we introduce explicit solvent particles into the system. These particles generate an effective osmotic pressure across the lipid bilayer, which can be finely tuned by varying the particle number density inside (ρ_{in}) and outside (ρ_{out}) the vesicle.

The solvent is composed of simple point-like particles modeled using a standard repulsive branch of Lennard-Jones (12-6) potential truncated at its minimum ($r_c = 2^{1/6}\sigma$) to ensure excluded volume interactions. The solvent particles interact with the membrane beads through the same truncated LJ potential.

5. Details on MD Simulations

To stabilize this initial configuration, we performed an energy minimization step in LAMMPS using the following command:

```
minimize 0.0 1.0e-8 1000 100000
```

Following the minimization procedure it is possible to start a NVT production run.

The molecular dynamics (MD) simulations were performed using the following system specifications and software environment:

Software:: LAMMPS (version 29 Aug 2024)

Operating System:: Linux “Ubuntu 24.04.3 LTS”

Compiler & Parallelization:: GNU C++ 11.4.0 with Open MPI v4.1.6

Installed optional LAMMPS packages:: DIPOLE, MOLECULE, EXTRA-FIX

Appendix C: Simulation snapshots

1. Self assembly and vesiculation

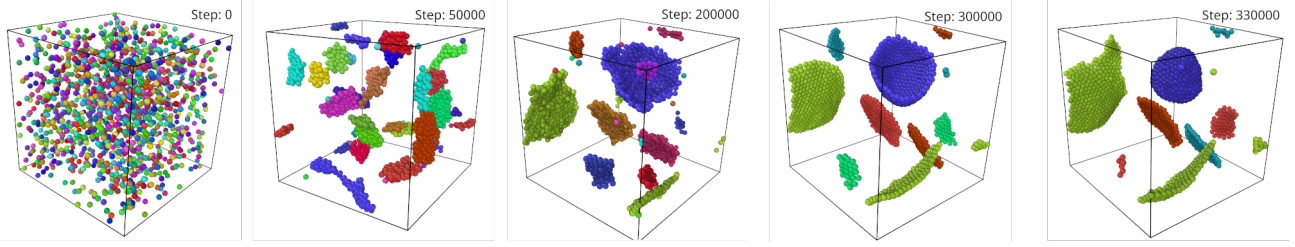


FIG. 13: Representative snapshots at $t = 500 \tau_{LJ}$ showing the effect of the tilt modulus k_{tilt} on self-assembly. For low k_{tilt} the system forms compact three-dimensional aggregates, while for higher k_{tilt} extended planar patches appear. Parameters: $k_{\text{splay}} = 1$, $\zeta = 5.0$, $w_c = 2.0\sigma$ and a cutoff radius $r_c = 2.5\sigma$.

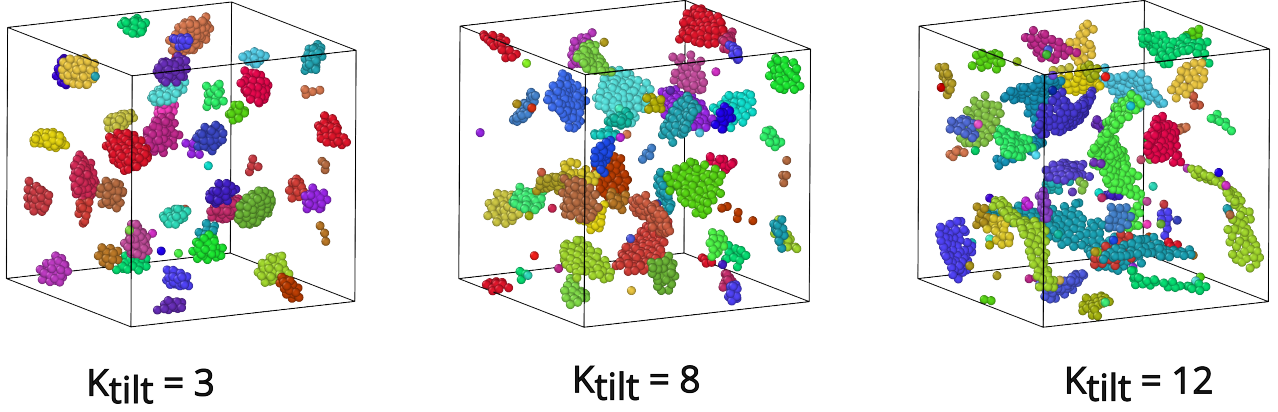


FIG. 14: Temporal snapshots of self assembly simulations at $t = 500 \tau_{LJ}$ across a range of tilt moduli. Parameters: $k_{\text{splay}} = 1$, $\zeta = 5.0$, $w_c = 2.0\sigma$ and a cutoff radius $r_c = 2.5\sigma$.

Appendix D: Stability exploration

In Fig. 15 we represent the stability plot for different parameters set of the model.

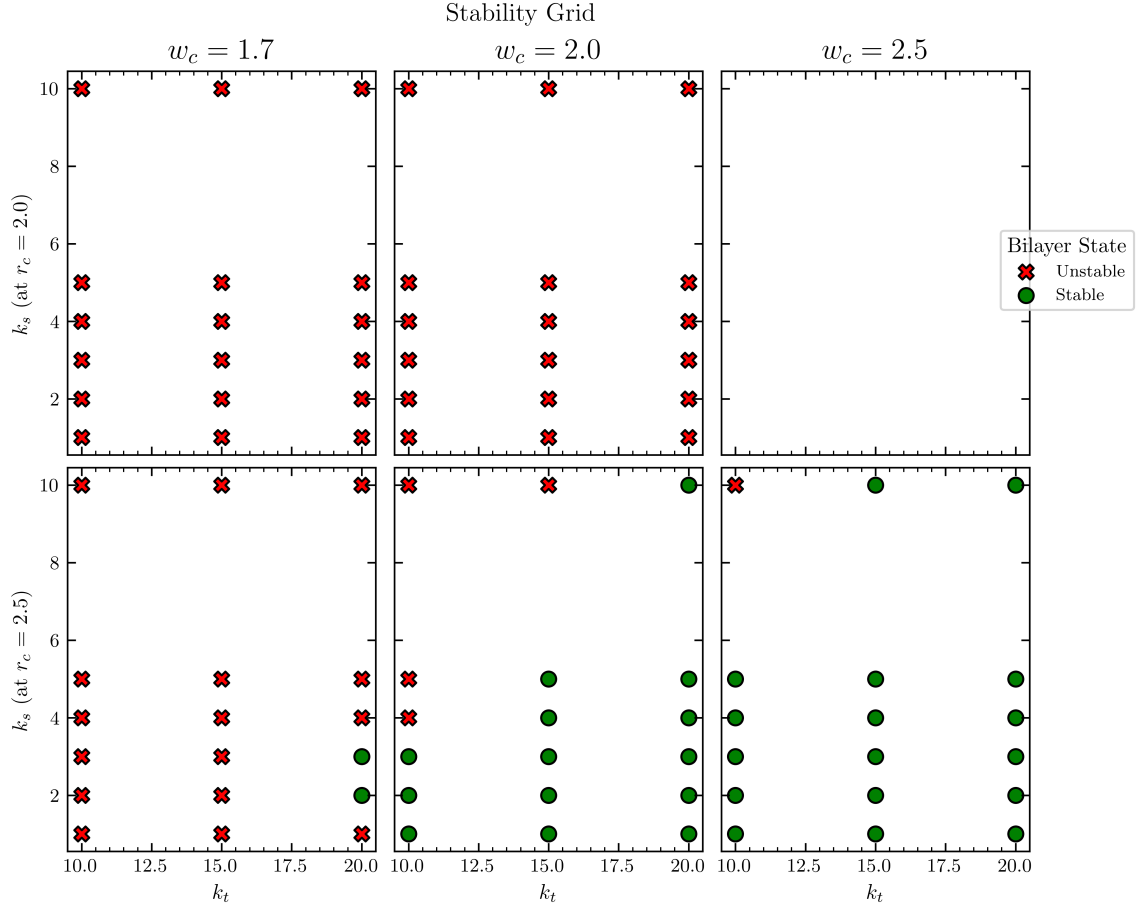


FIG. 15: Stability plot for different parameters set of the model.

Appendix E: Computational benchmark

To evaluate the parallel scalability of the simulation framework, benchmarking was performed on a planar square lattice membrane. The test system utilized an NVE ensemble under periodic boundary conditions.

We investigated the scaling behavior by sweep-sampling both the total particle count ($N \in \{400, 2500, 10k, 100k, 500k\}$) and the number of MPI tasks (CPU cores). Performance was quantified using the speedup $S_p = T_1/T_p$, where T_1 represents the execution time of the serial (1 CPU core) case. All benchmark were performed on a Linux workstation equipped with an AMD Ryzen Threadripper PRO 7985WX CPU (64 cores, 2 threads/core, 3.00 GHz) and 128 GB of RAM, using the LAMMPS configuration specified in section B 5.

Figure 16 illustrates the parallel speedup relative to the base configuration for various system sizes. The results highlight the transition from communication-bound regimes in smaller systems to computation-dominated regimes in larger systems, where the speedup more closely follows ideal linear scaling.

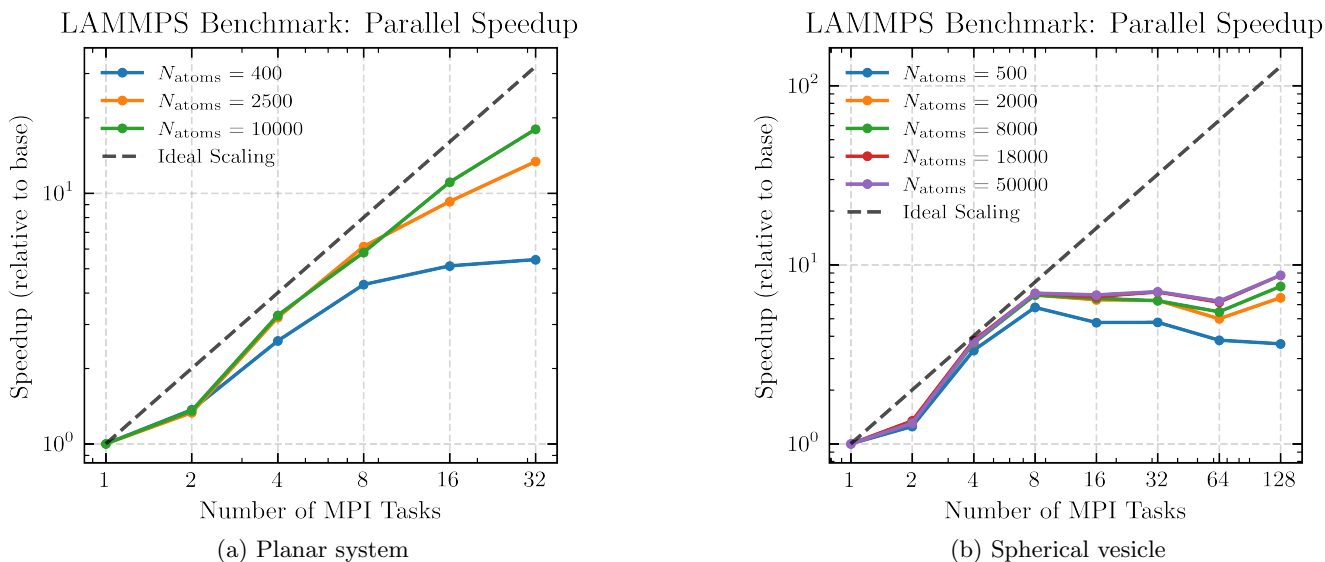


FIG. 16: Parallel speedup as a function of MPI tasks for varying system sizes. The dashed line represents ideal linear scaling.

Appendix F: Code and data Availability

The full codebase used for simulations and analysis is available on GitLab at <https://gitlab.tudelft.nl/idema-group/MesoMem>.

-
- [1] B. Alberts, ed., *Molecular Biology of the Cell*, 4th ed. (Garland Science, New York, 2002).
 - [2] F. Frey and T. Idema, More than just a barrier: Using physical models to couple membrane shape to cell function, *Soft Matter* **17**, 3533 (2021).
 - [3] K. B. Pedersen, H. I. Ingólfsson, D. P. Ramirez-Echemendia, L. Borges-Araújo, M. D. Andreasen, C. Empereur-mot, J. Melcr, T. N. Ozturk, W. F. D. Bennett, L. R. Kjølbye, C. Brasnett, V. Corradi, H. M. Khan, E. A. Cino, J. Crowley, H. Kim, B. Fábíán, A. C. Borges-Araújo, G. M. Pavan, G. Launay, F. Lolicato, T. A. Wassenaar, M. N. Melo, S. Thallmair, T. S. Carpenter, L. Monticelli, D. P. Tieleman, B. Schiøtt, P. C. T. Souza, and S. J. Marrink, The Martini 3 Lipidome: Expanded and Refined Parameters Improve Lipid Phase Behavior, *ACS Central Science* **11**, 1598 (2025).
 - [4] I. R. Cooke, K. Kremer, and M. Deserno, Tunable generic model for fluid bilayer membranes, *Physical Review E* **72**, 011506 (2005).
 - [5] A. Srivastava and G. A. Voth, Hybrid Approach for Highly Coarse-Grained Lipid Bilayer Models, *Journal of Chemical Theory and Computation* **9**, 750 (2013).

- [6] G. Gompper and D. M. Kroll, Membranes with Fluctuating Topology: Monte Carlo Simulations, *Physical Review Letters* **81**, 2284 (1998).
- [7] G. Dadunashvili and T. Idema, Flippy: User friendly and open source framework for lipid membrane simulations (2023), arXiv:2303.12305 [cond-mat].
- [8] W. Pezeshkian and J. H. Ipsen, Mesoscale simulation of biomembranes with FreeDTS, *Nature Communications* **15**, 548 (2024).
- [9] H. Yuan, C. Huang, J. Li, G. Lykotraftitis, and S. Zhang, One-particle-thick, solvent-free, coarse-grained model for biological and biomimetic fluid membranes, *Physical Review E* **82**, 011905 (2010).
- [10] H. Noguchi, Solvent-free coarse-grained lipid model for large-scale simulations, *The Journal of Chemical Physics* **134**, 055101 (2011).
- [11] J. F. Dama, A. V. Sinitskiy, M. McCullagh, J. Weare, B. Roux, A. R. Dinner, and G. A. Voth, The Theory of Ultra-Coarse-Graining. 1. General Principles, *Journal of Chemical Theory and Computation* **9**, 2466 (2013).
- [12] H. Yuan, C. Huang, and S. Zhang, Dynamic shape transformations of fluid vesicles, *Soft Matter* **6**, 4571 (2010).
- [13] C. Vanhille-Campos and A. Šarić, Modelling the dynamics of vesicle reshaping and scission under osmotic shocks, *Soft Matter* **17**, 3798 (2021).
- [14] Z. Shen, H. Ye, X. Yi, and Y. Li, Membrane Wrapping Efficiency of Elastic Nanoparticles during Endocytosis: Size and Shape Matter, *ACS Nano* **13**, 215 (2019).
- [15] L. Harker-Kirschneck, B. Baum, and A. Šarić, Changes in ESCRT-III filament geometry drive membrane remodelling and fission in silico, *BMC Biology* **17**, 82 (2019).
- [16] H. Noguchi, Shape deformation of lipid membranes by banana-shaped protein rods: Comparison with isotropic inclusions and membrane rupture, *Physical Review E* **93**, 052404 (2016).
- [17] A. P. Thompson, H. M. Aktulga, R. Berger, D. S. Bolintineanu, W. M. Brown, P. S. Crozier, P. J. In 't Veld, A. Kohlmeyer, S. G. Moore, T. D. Nguyen, R. Shan, M. J. Stevens, J. Tranchida, C. Trott, and S. J. Plimpton, LAMMPS - a flexible simulation tool for particle-based materials modeling at the atomic, meso, and continuum scales, *Computer Physics Communications* **271**, 108171 (2022).
- [18] M. Hamm and M. Kozlov, Elastic energy of tilt and bending of fluid membranes, *The European Physical Journal E* **3**, 323 (2000).
- [19] M. Paesani and I. M. Ilie, Metaparticles: Computationally engineered nanomaterials with tunable and responsive properties, *The Journal of Chemical Physics* **161**, 244905 (2024).
- [20] P. F. Fahey and W. W. Webb, Lateral diffusion in phospholipid bilayer membranes and multilamellar liquid crystals, *Biochemistry* **17**, 3046 (1978).
- [21] R. Goetz, G. Gompper, and R. Lipowsky, Mobility and Elasticity of Self-Assembled Membranes, *Physical Review Letters* **82**, 221 (1999).
- [22] W. Helfrich and R. M. Servuss, Undulations, steric interaction and cohesion of fluid membranes, *Il Nuovo Cimento D* **3**, 137 (1984).
- [23] M. Muñoz Basagoiti, F. Frey, B. Meadowcroft, M. Amaral, A. Prada, and A. Saric, A tutorial for mesoscale computer simulations of lipid membranes: Tether pulling, tubulation and fluctuations, *Soft Matter* , 10.1039.D5SM00148J (2025).
- [24] M. F. Ergüder and M. Deserno, Identifying systematic errors in a power spectral analysis of simulated lipid membranes, *The Journal of Chemical Physics* **154**, 214103 (2021).
- [25] R. Dimova, Recent developments in the field of bending rigidity measurements on membranes, *Advances in Colloid and Interface Science* **208**, 225 (2014).
- [26] C. van der Wel, A. Vahid, A. Šarić, T. Idema, D. Heinrich, and D. J. Kraft, Lipid membrane-mediated attraction between curvature inducing objects, *Scientific Reports* **6**, 32825 (2016).
- [27] S. van der Ham, A. Brown, H. Kusumaatmaja, and H. R. Vutukuri, From shallow to full wrapping: Geometry and deformability dictate lipid vesicle internalization, *Nano Letters* **25**, 16451 (2025).
- [28] H. Deuling and W. Helfrich, The curvature elasticity of fluid membranes: A catalogue of vesicle shapes, *J. Phys. France* **37**, 1335 (1976).
- [29] U. Seifert, K. Berndl, and R. Lipowsky, Shape transformations of vesicles: Phase diagram for spontaneous-curvature and bilayer-coupling models, *Phys. Rev. A* **44**, 1182 (1991).
- [30] M. P. Allen and G. Germano, Expressions for forces and torques in molecular simulations using rigid bodies, *Molecular Physics* **104**, 3225 (2006).
- [31] V. A. Dahl, A. B. Dahl, and R. Larsen, Surface detection using round cut, in *2014 2nd International Conference on 3D Vision*, Vol. 2 (2014) pp. 82–89.